Applied Clay Science 296 (2027) 108445

Contents lists available at ScienceDirect

Applied Clay Science

journal homepage: www.elsevier.com/locate/clay

Research Paper

Pressure-induced structural evolution of halloysite: Influence of morphology and pressure-transmitting medium on water uptake

V. Balédent [a,b,*], J. Bodin [a], S. Rouzière [a], P. Launois [a], E. Joussein [c], E. Paineau [a]

[a] Université Paris-Saclay, CNRS, Laboratoire de Physique des Solides, 91405 Orsay, France
[b] Institut universitaire de France (IUF), Paris, France
[c] Université de Limoges, E2LIM UR 24133, 123 avenue Albert Thomas, 87060 Limoges, France

ARTICLE INFO

Keywords:
Halloysite
Pressure
Water intercalation

ABSTRACT

Halloysite belongs to the kaolinite subgroup but differs from other polymorphs by its morphology and the presence of interlayer water. Despite its growing technological relevance, the structural response of halloysite to high pressure remains poorly understood. Here, we investigate the pressure-induced structural evolution of halloysite using in situ X-ray diffraction in a diamond anvil cell up to ~7 GPa, focusing on the influence of particle morphology and pressure-transmitting medium. Two halloysite samples with distinct morphologies (spheroidal or cylindrical) were studied under both hydrated and dehydrated conditions, using water or silicone oil as pressure-transmitting media. The structural analysis reveals strongly morphology-dependent behavior. Spheroidal halloysite undergoes rapid and irreversible dehydration below 0.5 GPa, accompanied by an increase in stacking coherence. In contrast, cylindrical halloysite nanotubes exhibit pressure-induced water intercalation when compressed in an aqueous environment. Inserted water acts as a structural buffer manifesting by a compressibility plateau between 1.5 and 3 GPa. The bulk moduli, extracted from Birch–Murnaghan fits, range from ~29 to ~51 GPa depending on morphology, hydration state, and pressure-transmitting medium. Despite these distinct water behaviors, all samples ultimately exhibit a structural instability of the aluminosilicate framework at critical pressures between ~2.5 and 4.8 GPa. These findings demonstrate that halloysite morphology controls pressure-driven water intercalation, highlighting the coupled role of structural geometry and surrounding medium in governing the mechanical and hydration behavior of clay nanoparticles.

1. Introduction

The study of clay mineral structures is a multidisciplinary endeavor because of their considerable impact on natural and applied sciences. Clay minerals are responsible for numerous soil properties, including swelling/deswelling cycles and adsorption of pollutants (Zhou and Keeling, 2013; Otunola and Ololade, 2020), while their stability and biocompatibility make them valuable as pharmaceutically active compounds or as vectors for drug delivery (Viseras et al., 2010; Kiaee et al., 2022). Their polymorphic nature, supported by a layered structure with different sizes (length, diameter and interlayer spacing), and their low cost naturally offer extensive potential applications in areas such as gas or pollutant storage and filtration (Churchman et al., 2006; Volzone, 2007; Ewis et al., 2022). Consequently, clay minerals are compounds of significant interest in various fields, including geology, medicine, and climate science.

Pressure has long been a subject of great interest, as it can drive many remarkable phenomena such as structural transformations and subsequent property modifications, polymerization, or the formation of new polymorphs (McMahon, 2012). Widely used on different nanostructures (carbon, silica, oxides, etc.), in situ X-ray scattering experiments under pressure are rarely carried out on clay minerals to investigate their structural properties under extreme conditions (Lee et al., 2020; Hwang et al., 2017), in contrast to spectroscopic experiments (Butler and Frost, 2006; Basu and Mookherjee, 2021). Pressure-induced water intercalation has been reported in synthetic trioctahedral Na-fluorohectorite nanosheets (You et al., 2013) and more recently in chrysotile nanotubes (Goryainov et al., 2021). The use of a Diamond Anvil Cell (DAC) also provides convenient access to the mechanical properties of nanoparticles. Pressure-induced radial deformations and axial compressibility have been systematically studied in synthetic aluminosilicate and aluminogermanate imogolite clay nanotubes (Rouzière et al., 2023, 2024), concluding in irreversible collapse of the single-wall nanotubes at moderate pressures ($P \leq 5$ GPa), depending on the pressure transmitting medium (PTM) and the nanotube structure.

* Corresponding author at: Université Paris-Saclay, CNRS, Laboratoire de Physique des Solides, 91405 Orsay, France.
E-mail address: victor.baledent@universite-paris-saclay.fr (V. Balédent).

https://doi.org/10.1016/j.clay.2026.108445
Received 3 June 2026; Received in revised form 21 October 2026; Accepted 25 October 2026
Available online 7 November 2026
0169-1317/© 2026 Elsevier B.V. All rights are reserved, including those for text and data mining, AI training, and similar technologies.

The kaolinite subgroup is one of the most representative phyllosilicates on the Earth's surface, including kaolinite, dickite, nacrite and halloysite polymorphs. These clay minerals have a 1:1 dioctahedral structure with an ideal chemical composition $Al_2Si_2O_5(OH)_4$, except for halloysite, which can contain up to 2 water molecules per structural unit. Dera et al. demonstrated an isosymmetric displacive structural transformation in 1:1 layers to explain the structural transition of dickite above 2 GPa under hydrostatic conditions (Dera et al., 2003). Welch and Crichton (2010) investigated the compressional behavior of kaolinite under static compression at room temperature, demonstrating two new kaolinite polytypes at ~3.7 and 7 GPa with a change in the stacking vector sequence of the aluminosilicate sheets with respect to the ambient polytype. In addition, reversible pressure-induced water intercalation between kaolinite layers has been reported under conditions mimicking cold subduction zones ($P \leq 2.5$ GPa, $T = 200°C$) (Hwang et al., 2017). By contrast, an irreversible water intercalation was observed in the 1:1 structure of nacrite upon compression (Hwang et al., 2020).

Much less attention has been paid to the pressure-induced transformations of halloysite, which differs from the other kaolin polymorphs by its morphology (tubular or spheroidal particles) and by the presence of water molecules that are naturally intercalated in the interlayer spacing between the 1:1 sheets (Joussein et al., 2005). Halloysite occurs widely in both weathered rocks and soils around the world. Over the past fifteen years, there has been increasing research interest in its potential applications as fillers in various polymeric matrices, controlled drug delivery, carriers for the supply and sustained release of active agents, uptake of contaminants, battery technology and photo(electro)catalysis (Yuan et al., 2015; Zhang et al., 2021; Naciri et al., 2024; Calvino et al., 2025).

The hydrated halloysite is characterized by an interlayer spacing d = 10 Å, which led to its being named halloysite-(10 Å). The hydrated form of halloysite easily and irreversibly loses its interlayer water, giving rise to halloysite-(7 Å) when exposed to dry air, vacuum, or upon heating (Siranidi et al., 2024). In this article, we report the first investigation of the pressure-induced structural evolution of halloysite with distinct morphologies, namely spheroidal and cylindrical halloysite, up to ~7 GPa. Using in situ X-ray diffraction under pressure, we demonstrate how the pressure-transmitting medium (water vs. silicone oil) modulates the structural changes, since the samples contain water molecules trapped within their interlayer space.

2. Experimental methods

2.1. Sample preparation

Two halloysite reference samples with different morphologies were selected. Halloysite from Dragon Mine (Utah, USA) was purchased from Sigma Aldrich, while the second halloysite sample from Opotiki (New Zealand) was kindly provided by Imerys. Halloysite from Dragon Mine consists of nanotubes with predominantly cylindrical shapes (Hillier et al., 2016), whereas the Opotiki sample is composed solely of spheroidal halloysite (Churchman et al., 1984). A low-defective kaolinite sample (KGa-1b) was supplied by The Clay Mineral Society (Warren County, Georgia). For all samples, the sub-2 μm clay fraction was collected by sedimentation under gravity according to Stokes' law after NaCl (1 mol L^{-1}) saturation. Representative SEM images of pristine samples are provided in the Appendix (Fig. 6), confirming the respective cylindrical and spheroidal morphologies of halloysites.

2.2. Ambient-condition characterization and lattice parameter extraction

Prior to this study, halloysite powders were characterized by X-ray diffraction (XRD) at ambient pressure on the MORPHEUS platform at the Laboratoire de Physique des Solides (LPS), using an experimental diffraction setup equipped with an X-ray molybdenum (λ = 0.71 Å) rotating anode generator (RU200, Rigaku). Powders were filled into borosilicate glass capillaries of 1 mm diameter (WJM-Glas, Müller GmbH). XRD patterns were collected on a two-dimensional large-area detector (MAR345, marXperts GmbH) with 150 μm pixel size, the sample-to-detector distance being fixed at 250 mm. The intensity as a function of the scattering wavevector Q ($Q = \frac{4\pi}{\lambda}\sin\theta$, with 2θ the scattering angle) was obtained by angular integration of the two-dimensional patterns using a home-made software. The diffractograms of naturally hydrated powders and of powders dehydrated at 200°C for 2 h (dehydration performed ex situ, in a laboratory oven, prior to loading) are shown in Fig. 1. The patterns exhibit a first reflection at 0.85 $Å^{-1}$, indexed as the 001 reflection. It corresponds to an interlayer spacing $d_{interlayer}$ = 7.4 Å, also illustrated in the same figure. In the presence of interlayer water, this reflection shifts to around 0.63 $Å^{-1}$, corresponding to a spacing d_{H_2O} of 10 Å, as it is seen for naturally hydrated spherical halloysite. Note that it is not fully hydrated: there is a coexistence of hydrated and non-hydrated zones. Importantly, the addition of water to the powder of pristine samples — which mimics the aqueous PTM — does not induce the insertion of additional water molecules between the layers of both pristine halloysite samples (see Fig. 7 in Appendix).

While kaolinite can be indexed in a monoclinic space group with a well-defined three-dimensional long-range order (Hwang et al., 2017), this is not the case for halloysite (Pan et al., 2026). The prominent features at Q = 1.4 and 2.4 $Å^{-1}$ correspond to the 02,11 and 20,13 in-plane bands, respectively, and allow the determination of the lattice parameters a and b. Such indexation has already been employed in a previous study (Pan et al., 2026). The asymmetric shape of the 02, 11 and 20, 13 bands traduces random stacking of the curved kaolinite sheets (Warren, 1941; Bousige et al., 2012; Monet et al., 2018). The bands maxima are located slightly beyond the positions that the Bragg reflections at 020, 110, and 200,130 would occupy. The values of the parameters a and b should, in principle, be determined by fitting the band profile to appropriate cylindrical or spherical stacking models. Such a detailed analysis is beyond the scope of this study, where a and b values were simply deduced from the maxima of the 02, 11 and 20, 13 bands, respectively. The obtained value are thus slightly overestimated, as can be observed in Table 1 when comparing these values to those obtained for kaolinite. The average unit cell volume is given by the area of the rectangular (a, b) unit multiplied by the interlayer spacing c, which is calculated from the position of the 001 reflection. Consequently, it represents the mean volume occupied by a cell, rather than a genuine crystallographic elementary unit cell volume. The correlation length ξ_c of the c-axis stacking is deduced from the full width at half maximum Δq of the 001 reflection fitted with a Gaussian function: $\xi = \frac{2\pi}{\Delta q}$.

2.3. High-pressure X-ray diffraction

For each experiment, powder samples were loaded in a membrane-driven diamond anvil cell (DAC) using a copper–beryllium gasket, with either silicone oil (PDMS) or water as the pressure-transmitting medium (PTM). A small amount of gold powder was placed inside the DAC sample chamber to monitor pressure. The gold lattice parameter was extracted from the refinement of the gold diffractogram, and the pressure was determined using the third-order Birch–Murnaghan equation of state with V_0 = 67.847 $Å^3$, B_0 = 167 GPa, and B_0' = 5.5 taken from Ref. Boettger et al. (2012). X-ray diffractograms were recorded using the high-pressure diffraction setup developed at the Laboratoire de Physique des Solides (Orsay, France). The diffractometer utilizes a microfocus Mo X-ray tube (Incoatec GmbH) equipped with a Montel multilayer focusing optics, providing a monochromatic (λ = 0.711 Å) beam with a spot size of 100 μm and a divergence of 0.5 mrad at the sample position. The diffracted intensity is collected by a large-area MAR345 detector (MarXperts GmbH) and radially integrated to obtain the diffractogram using the Dioptas software (Prescher and Prakapenka,

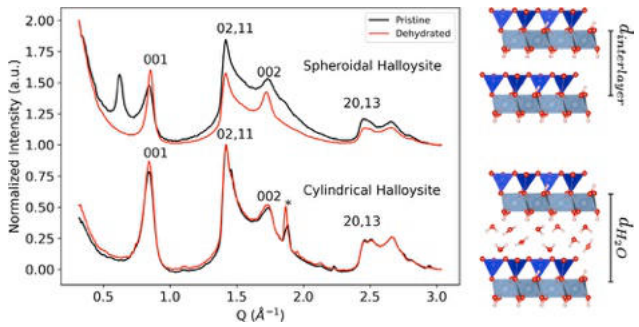

Fig. 1. X-ray diffraction patterns measured at ambient pressure of spheroidal and cylindrical halloysite pristine samples (in black) and after dehydration (in red). The diffractograms are vertically offset for clarity. The star symbol indicates a quartz impurity reflection. The scheme illustrates the Si–Al–O layers with or without intercalated water; Si, Al, O and H atoms are represented in blue, blue-gray, red and pink, respectively.

2015). It covers a wavevector range from 0.05 to 6.1 Å^{-1}. The exposure time was 30 min on the sample position and 2 min on the gold position at each pressure. The bulk modulus B_0 is determined using the second-order Birch–Murnaghan equation of state:

$$P(V) = \frac{3B_0}{2}\left[\left(\frac{V_0}{V}\right)^{\frac{7}{3}} - \left(\frac{V_0}{V}\right)^{\frac{5}{3}}\right] \quad (1)$$

where V is the volume under compression of the water-free unit cell, as defined in the experimental methods section, V_0 the volume at zero pressure, and B_0 the bulk modulus.

Throughout this article, the intensity of the reflections associated with the hydrated (0.63 Å^{-1}) and anhydrous (0.85 Å^{-1}) interlayer spacings is used as a proxy for the relative population of hydrated and dehydrated interlayer domains. This intensity-based approach is not free of ambiguity, since preferred orientation, reflection broadening, and pressure-induced disorder can also affect diffracted intensities. Two aspects of the present dataset mitigate this concern. First, all patterns are obtained by full azimuthal (360°) integration of the two-dimensional diffraction images, which strongly averages out contributions from preferred orientation compared to a limited-azimuth integration. Second, the two reflections monitored are both 00*l*-type reflections along the same stacking direction and should, to first order, respond similarly to a given change in texture or stacking disorder; their strictly anti-correlated intensity evolution (Figs. 2a, 4a) is therefore more consistent with a genuine population transfer between hydrated and dehydrated interlayer domains than with an orientation artifact. Under the simplifying assumption of a two-population (hydrated/dehydrated) mixture with comparable structure factors, the intensity ratio $I_{H_2O}/(I_{H_2O}+I_{anhydrous})$ can further be interpreted as a semi-quantitative proxy for the hydrated volume fraction. A full quantitative Rietveld-type phase-fraction refinement is, however, beyond the reach of the present turbostratically disordered samples, and the intensity variations reported below should accordingly be read as a qualitative-to-semi-quantitative indicator of hydration state, not as an absolute water content.

We note that, among the runs performed with water as the PTM, reflections from the ice-VI/VII phases of the excess (bulk) water are clearly resolved in some diffractogram color maps (Figs. 10 and 13) but not in others (Figs. 9 and 14), even though all loadings were prepared following the same protocol. We attribute this to the small beam size (100 μm) used in this study relative to the lateral extent of the sample chamber: the exact proportion of clay powder versus free PTM sampled by the beam depends sensitively on its precise position within the chamber, so that a small lateral offset can be sufficient to probe a region with little free water, without this reflecting the true water content of the chamber as a whole. This is consistent with the fact that, within a given loading, the pattern collected at the gold marker position — located elsewhere in the chamber and used solely for pressure calibration — does not necessarily show ice reflections even in the case where it is observed on sample position. A preliminary run (not included in the main dataset) on naturally hydrated cylindrical halloysite in water, in which ice-VI/VII reflections were likewise not resolved, showed a pressure-induced structural evolution fully consistent with the results reported below, indicating that the presence or absence of resolvable ice reflections has little if not zero impact on the observations reported here.

3. Results

The high-pressure structural evolution of halloysite was investigated by systematically varying particle morphology, initial hydration state, and the nature of the pressure-transmitting medium (PTM). Kaolinite was also studied as a reference for the behavior of lamellar 1:1 phyllosilicates under pressure. While the complete set of experimental diffractograms and detailed systematic measurements for each sample are provided in the Appendix, the following sections focus on the key results necessary to draw the main structural conclusions.

3.1. Kaolinite

We first investigated kaolinite as a function of pressure using water as the transmitting medium. This study serves both to characterize the behavior of the parent compound of the halloysite family and to compare with the results reported by Hwang et al. (2017). The kaolinite structure is triclinic, but since the angles α and γ are very close to 90° (91.7° and 89.8°, respectively), we approximated a monoclinic cell for the Le Bail refinement, as our experimental resolution is insufficient to refine all six parameters independently. The lattice parameters obtained at ambient pressure are a = 5.09 ± 0.01 Å, b = 8.82 ± 0.01 Å, c = 7.37 ± 0.01 Å and β = 105.5 ± 0.1° (Table 1), in close agreement with those reported by Hwang et al. (2017): a = 5.16 Å, b = 8.94 Å, c = 7.40 Å and β = 104.9°. Similarly, the pressure evolution is consistent with previous results. We observe a first structural transition at P_C = 4.0 ± 0.1 GPa (Table 1), comparable to the 3.6 GPa reported by Hwang et al. and a second transition is observed near 7 GPa also. Note that the fingerprint of the first transition at P_C is characterized by the merging of the 2.5 and 2.7 Å^{-1} reflections (see Fig. 8). The bulk modulus obtained from the second-order Birch–Murnaghan equation is B_0 = 55 ± 1 GPa (Table 1), in good agreement with the value of 58.8 ± 0.4 GPa reported (Hwang et al., 2017). These transition pressures are also consistent with two independent Raman spectroscopy studies of kaolinite published since the XRD study of Hwang et al. (2017): Basu et al. (2023) report a K-I → K-II transition at ~2.9 GPa and a K-II → K-III transition at ~6.1 GPa, while Hong et al. (2022) independently report transitions at 2.9 and 6.5 GPa combining Raman scattering and electrical conductivity. The somewhat lower transition pressures obtained by these vibrational (local, hydrogen-bond-sensitive) probes compared to our XRD values (4.0 and ~7 GPa) is consistent with such probes typically detecting the onset of structural change before it is resolved as a long-range lattice transition by diffraction.

3.2. Spheroidal halloysite: Pressure-induced dehydration and compressibility

3.2.1. Naturally hydrated samples

Spheroidal halloysite, which is naturally hydrated, exhibits a diffraction reflection at 0.63 Å^{-1} corresponding to the interlayer spacing in the presence of water (d_{H_2O} ≈ 10 Å at ambient pressure, Table 1). When water is used as the PTM, the intensity of this reflection

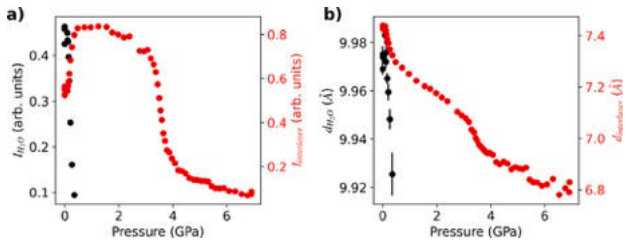

Fig. 2. Water desorption in spheroidal halloysite under pressure. (a) Pressure dependence of the intensity of the diffraction reflections associated with the hydrated interlayer spacing at 0.63 Å^{-1} (black circles, left axis) and with the anhydrous interlayer spacing at 0.85 Å^{-1} (red circles, right axis). (b) Pressure evolution of the interlayer distance with (black circles, left axis, d_{H_2O}) and without (red circles, right axis) water between the layers. Water was used as the pressure-transmitting medium.

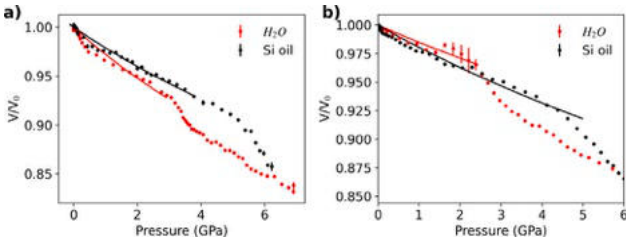

Fig. 3. Pressure evolution of the unit cell volume of spheroidal halloysite, normalized to its ambient-pressure value, with water (red points) or silicone oil (PDMS, black points) as the pressure-transmitting medium, for: (a) naturally hydrated samples and (b) dehydrated samples. Solid lines are fits to the data below P_C using the second-order Birch–Murnaghan equation of state.

decreases rapidly with increasing pressure (Fig. 2a), indicating early-stage expulsion of interlayer water. The reflection has completely vanished by 0.4 GPa. Simultaneously, the intensity of the reflection at 0.85 Å^{-1}, corresponding to the anhydrous interlayer spacing, increases, confirming that the expulsion of water leads to a collapse of the interlayer to the dehydrated configuration. The interlayer distance itself, related to the reflection's position, decreases monotonically with pressure, but the compression of d_{H_2O} amounts to only 0.6% before dehydration, compared to nearly 2% for the anhydrous interlayer spacing over the same pressure range [0:0.4] GPa (see Fig. 2b). This indicates that the presence of interlayer water significantly reduces the compressibility of spheroidal halloysite along the stacking direction. At higher pressure, a structural transition is observed that is very similar to the one observed for kaolinite, at P_C = 3.1 GPa.

When PDMS is used as the PTM, the hydrated reflection at 0.63 Å^{-1} persists to higher pressures and remains observable up to 6 GPa. This is consistent with the working hypothesis, discussed further in Section 4.1, that PDMS limits water expulsion from the interlayer space. The structural transition pressure P_C is therefore shifted: it occurs at 3.1 ± 0.1 GPa with water as PTM and at 3.9 ± 0.1 GPa with PDMS (Table 1). This can be rationalized by the observation that the presence of interlayer water, sustained over a wider pressure range in PDMS, stiffens the structure and delays the onset of the structural instability. Consistently, the bulk modulus (always calculated on the water-free unit cell volume) is lower in the water PTM case (B_0 = 33 ± 1 GPa) than in the PDMS case (B_0 = 45 ± 1 GPa), as shown in Fig. 3 and reported Table 1.

3.2.2. Effect of dehydration

When spheroidal halloysite is pre-dehydrated, the reflection at 0.63 Å^{-1} is absent. The in-plane lattice parameters (*a*, *b*) remain essentially unchanged with respect to the hydrated form, but the interlayer spacing decreases by ~3%, from ~7.49 Å in the hydrated state to ~7.25–7.28 Å in the dehydrated state (Table 1). This small contraction in the interlayer distance may suggest that a trace amount of water is present between the layers of the supposedly anhydrous region, which is then desorbed during heat treatment. This hypothesis is further reinforced by the fact that the heat treatment considerably increases the correlation length along the *c*-axis by 50% (from 80 to 120 Å) as shown in Figs. 9e and 10d. This more compact initial structure results in a higher resistance to compression: the bulk modulus increases significantly, reaching B_0 = 51 ± 2 GPa (water PTM) and B_0 = 50 ± 1 GPa (PDMS), compared to 33 and 45 GPa for the hydrated samples, respectively (Table 1). The structural transition pressure is lower for dehydrated samples (P_C = 2.5 ± 0.1 GPa with water and 4.8 ± 0.1 GPa with PDMS, Table 1), reflecting the fact that the absence of water makes the structure intrinsically more rigid but also potentially more brittle. Importantly, the bulk moduli of the dehydrated spheroidal samples are almost identical regardless of the PTM.

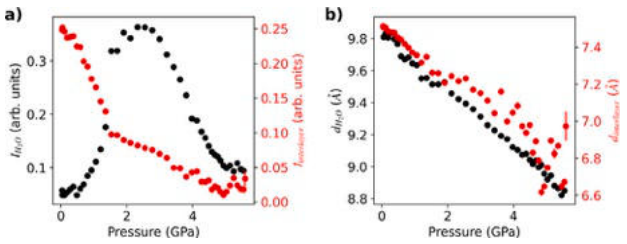

Fig. 4. Anomalous compression and water intercalation in cylindrical halloysite nanotubes. (a) Pressure dependence of the intensity of the diffraction reflection associated with the hydrated interlayer spacing (black circles, left axis) and with the anhydrous interlayer spacing (red circles, right axis). (b) Pressure evolution of the interlayer distance with (black circles, left axis, d_{H_2O}) and without (red circles, right axis) interlayer water. Water was used as the pressure-transmitting medium.

3.3. Cylindrical halloysite: Pressure-induced water intercalation

Cylindrical halloysite (nanotubes) exhibits a markedly different phenomenology, characterized by the active insertion of water under pressure when an aqueous reservoir is available.

3.3.1. Anomalous compression and water uptake

In contrast to the spheroidal case, the hydrated reflection of cylindrical halloysite (associated with d_{H_2O} ≈ 10 Å at ambient pressure, Table 1) shows a dramatic increase in intensity upon compression with water as PTM, reaching a maximum around 1.5 GPa. Simultaneously, the intensity of the anhydrous interlayer reflection decreases, indicating that water progressively fills interlayer spaces that were initially free of water (Fig. 4a). This constitutes direct evidence of pressure-induced water intercalation at room temperature, analogous to that reported by Hwang et al. (2017). Interestingly, the compressibility of the hydrated and anhydrous interlayer distances shows only a subtle anomaly around this pressure (Fig. 4b), suggesting that the water intercalation acts primarily as an intensity redistribution between the two structural populations rather than inducing a strong modification of the *c*-axis compressibility.

The water-free volume evolution as a function of pressure, calculated on the non hydrated fraction, reveals a structural transition at P_C = 3.7 ± 0.1 GPa with water as PTM and at P_C = 3.3 ± 0.1 GPa with PDMS (Table 1). The bulk modulus extracted from the Birch–Murnaghan fit is B_0 = 30 ± 1 GPa (water) and B_0 = 39 ± 1 GPa (PDMS), as shown in Fig. 5. These values are somewhat lower than those of the corresponding spheroidal samples, consistent with the open-ended tubular geometry being inherently more susceptible to radial deformation.

Table 1
Summary of the structural and mechanical properties of the halloysite samples and kaolinite reference. For kaolinite, the lattice parameters a, b, c, and β correspond to a monoclinic cell refinement, and $d_{\text{interlayer}}$ is the interlayer distance accounting for the monoclinic angle β. For halloysite samples, a, b, and c are determined as described in the Experimental Methods section, where c corresponds to the interlayer distance in the absence of interstitial water. d_{H_2O} denotes the interlayer distance in the presence of interlayer water. P_C is the critical structural transition pressure, and B_0 is the bulk modulus derived from second-order Birch–Murnaghan equation of state fits below P_C. For spheroidal and cylindrical halloysite, columns are ordered as follows: naturally hydrated with H_2O, naturally hydrated with PDMS, dehydrated with H_2O, and dehydrated with PDMS. Values in parentheses represent the standard uncertainty on the last digit.

Shape	Layered	Spheroidal				Cylindrical			
Treatment	None	None		Dehydrated		None		Dehydrated	
PTM	H_2O	H_2O	PDMS	H_2O	PDMS	H_2O	PDMS	H_2O	PDMS
a (Å)	5.09 (0.01)	5.12 (0.01)	5.12 (0.01)	5.12 (0.01)	5.12 (0.01)	5.11 (0.01)	5.11 (0.01)	5.11 (0.01)	5.11 (0.01)
b (Å)	8.82 (0.01)	8.85 (0.01)	8.86 (0.01)	8.85 (0.01)	8.84 (0.01)	8.83 (0.01)	8.84 (0.01)	8.82 (0.01)	8.81 (0.01)
c (Å)	7.37 (0.01)	7.44 (0.01)	7.49 (0.01)	7.25 (0.01)	7.28 (0.01)	7.51 (0.01)	7.47 (0.01)	7.25 (0.01)	7.25 (0.01)
β (°)	105.5 (0.1)	–	–	–	–	–	–	–	–
V (Å^3)	318.8 (0.3)	337.1 (0.3)	339.8 (0.3)	328.0 (0.3)	329.1 (0.3)	338.8 (0.4)	337.2 (0.3)	326.9 (0.3)	326.1 (0.3)
$d_{interlayer}$ (Å)	7.10 (0.01)	–	–	–	–	–	–	–	–
d_{H_2O} (Å)	–	9.97 (0.01)	9.98 (0.01)	–	–	9.87 (0.01)	–	–	–
P_c (GPa)	4.0 (0.1)	3.1 (0.1)	3.9 (0.1)	2.5 (0.1)	4.8 (0.1)	3.7 (0.1)	3.3 (0.1)	3.5 (0.1)	2.9 (0.1)
B_0 (GPa)	55 (1)	33 (1)	45 (1)	51 (2)	50 (1)	30 (1)	39 (1)	46 (1)	29 (1)

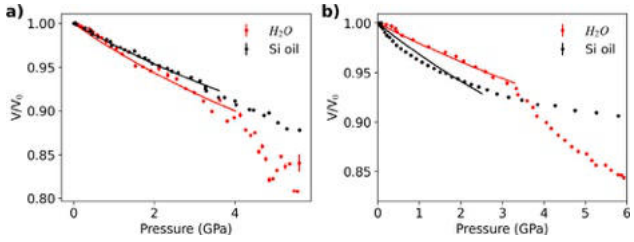

Fig. 5. Pressure evolution of the unit cell volume of cylindrical halloysite, normalized to its ambient-pressure value, with water (red points) or silicone oil (PDMS, black points) as the pressure-transmitting medium, for: (a) naturally hydrated samples and (b) dehydrated samples. Solid lines are fits to the data below P_C using the second-order Birch–Murnaghan equation of state.

3.3.2. *Effect of dehydration*

Upon dehydration, the interlayer spacing of cylindrical halloysite decreases by ~3%, from ~7.47–7.51 Å in the hydrated state to ~7.25 Å (Table 1), in close analogy to the spheroidal case. The compressibility increases accordingly: the bulk modulus rises to B_0 = 46 ± 1 GPa (water) and B_0 = 29 ± 1 GPa (PDMS) for the dehydrated cylindrical samples (Table 1). The structural transition pressures are P_C = 3.5 ± 0.1 GPa (water) and P_C = 2.9 ± 0.1 GPa (PDMS), comparable to those of the naturally hydrated counterparts. Notably, in the PDMS case, dehydration leads to a lower B_0 compared to the hydrated sample, suggesting that the absence of interlayer water in a non-aqueous medium suppresses the stiffening contribution of the interlayer medium.

4. Discussion

The results presented above establish that halloysite morphology is the primary factor governing the direction, magnitude, and pressure range of water content in halloysite under compression. The following discussion synthesizes the structural data, the water displacement (Figs. 2 and 4), and the mechanical properties (Table 1) to identify the key physical mechanisms at play.

4.1. *Morphology-controlled water intercalation: exhaling vs. inhaling*

The most striking contrast between the two halloysite morphologies lies in their response to an aqueous environment under pressure. Spheroidal halloysite behaves as an *exhaling* system: interlayer water is rapidly and irreversibly expelled below 0.5 GPa regardless of the PTM, although the rate and completeness of this process depends on the surrounding medium. The removal of interlayer water leads to a measurable increase in stacking coherence, as the collapse of the aluminosilicate sheets becomes more ordered in the absence of water layers. This is measured by the stacking correlation length, deduced from the inverse of the width of the 001 reflection (Fig. 9e), which increases from 85 to 103 Å between 0 and 0.4 GPa for water as PTM.

Cylindrical halloysite nanotubes, on the contrary, behave as an *inhaling* system: when an aqueous reservoir is available, compression actively drives water intercalation between layers that were initially free of water, with the hydrated population peaking around 1.5 GPa. This behavior is reminiscent of the pressure-induced water intercalation reported in kaolinite (Hwang et al., 2017) and in nacrite (Hwang et al., 2020), but occurs here at room temperature, pointing to the unique role of nanotube geometry in facilitating water uptake. The open-ended morphology of the nanotubes likely provides low-resistance pathways for water to enter the interlayer space under mechanical load, a mechanism that is geometrically suppressed in closed spheroidal shape. We emphasize that this pressure-induced water intercalation is a genuinely coupled phenomenon, requiring the simultaneous combination of (i) mechanical compression, (ii) the availability of an external aqueous reservoir, and (iii) the open-ended nanotube morphology; none of these three ingredients is sufficient on its own, as directly demonstrated by our ambient-pressure control experiment (Fig. 7, Appendix B) showing that simple contact with water, without compression, does not induce additional interlayer water uptake in either morphology.

The role of the PTM is secondary but significant in both cases. Despite the absence of direct microscopic evidence of a continuous PDMS layer around the particles, we propose the following explanation that in PDMS, the polymer chains may infiltrate interparticle spaces and mechanically encapsulate the particles, limiting the exchange of interlayer water with the surrounding medium. An alternative, non-exclusive explanation is kinetic rather than static: PDMS has a dynamic viscosity roughly two orders of magnitude larger than that of water, and this viscosity increases further under pressure; because water must diffuse out of the powder bed and through the surrounding medium within the finite exposure time of each pressure point (tens of minutes), the much slower diffusion kinetics expected in the highly viscous PDMS could by itself delay the apparent dehydration/rehydration equilibrium, independently of whether a literal encapsulating layer is present. Discriminating between these two hypotheses would require dedicated time-resolved measurements at fixed pressure, beyond the scope of the present study. For spheroidal halloysite, this results in the retention of interlayer water to higher pressures, shifting P_C from 3.1 GPa (water) to 3.9 GPa (PDMS) for naturally hydrated samples (Table 1). For cylindrical halloysite compressed in PDMS, the absence of an aqueous

reservoir prevents pressure-induced intercalation, and the structural response is closer to that of the dehydrated state.

4.2. Mechanical properties: the role of interlayer water and pressure-transmitting medium

The bulk moduli extracted from the Birch–Murnaghan fits (Table 1) reveal a consistent picture: the presence of interlayer water systematically softens the structure, while dehydration stiffens it. For spheroidal halloysite, B_0 increases from 33 GPa (hydrated, water PTM) to 51 GPa (dehydrated, water PTM). For cylindrical halloysite, the corresponding values are 30 GPa (hydrated, water PTM) and 46 GPa (dehydrated, water PTM). This stiffening effect upon dehydration is consistent with the reduced interlayer spacing (c decreasing from ~7.47–7.51 Å to ~7.25 Å), which leaves less room for further compression.

Comparing the two morphologies under equivalent conditions, spheroidal halloysite is systematically stiffer than cylindrical halloysite: for instance, in the hydrated state with water PTM, $B_0 = 33 \pm 1$ GPa (spheroidal) vs. 30 ± 1 GPa (cylindrical), and in the hydrated state with PDMS PTM, $B_0 = 45 \pm 1$ GPa (spheroidal) vs. 39 ± 1 GPa (cylindrical). These differences correspond respectively to about 2σ and 4σ of the combined statistical uncertainty ($\sigma_{comb} = \sqrt{1^2 + 1^2} \approx 1.4$ GPa), and are therefore statistically resolved, more clearly so for the PDMS comparison. This trend is consistent with the notion that the closed-shell geometry of spheroids provides higher resistance to hydrostatic stress than the open-ended tubular structure, which is inherently subject to greater radial deformation under pressure.

The bulk moduli of all halloysite samples (29–51 GPa, Table 1) are somewhat lower than that of kaolinite (55 GPa), which is consistent with the halloysite structure being less ordered along the stacking direction and more susceptible to non-hydrostatic strain. All values remain in the range reported for other 1:1 phyllosilicates (Hwang et al., 2017; Welch and Crichton, 2010).

We note, however, that the PTM dependence of B_0 is not systematic across hydration states for the cylindrical morphology. For the naturally hydrated cylindrical sample, B_0(PDMS) > B_0(water) (39 vs. 30 GPa), consistent with the general picture above: in PDMS, no external aqueous reservoir is available, and the sample behaves mechanically closer to a dehydrated (stiffer) nanotube than its water-PTM counterpart, which actively takes up additional water and is correspondingly softer. For the pre-dehydrated cylindrical sample, the trend is reversed, B_0(water) = 46 GPa > B_0(PDMS) = 29 GPa, and is not simply the mirror image of the hydrated case. This reversal remains an open question: it illustrates that the mechanical response of the open-ended nanotube geometry to hydration state and PTM is more complex than a simple, monotonic "water softens/dehydration stiffens" picture, in contrast with the more systematic trend observed for the closed-shell spheroidal morphology. Resolving its origin will require dedicated follow-up measurements, such as azimuthally resolved reflection-width analysis to probe stress anisotropy or an independent spectroscopic probe of residual interlayer water content.

4.3. Structural instability of the aluminosilicate framework

Despite the divergent water displacement at low-to-intermediate pressures, all samples ultimately undergo a structural instability of the aluminosilicate framework, evidenced by an abrupt change in the diffraction pattern at a critical pressure P_C. These pressures range from 2.5 to 4.8 GPa across all conditions (Table 1). The lowest P_C values are observed for dehydrated spheroidal halloysite in water (2.5 GPa), while the highest occurs also for dehydrated spheroidal halloysite in PDMS (4.8 GPa). This apparent paradox — dehydration both lowers and raises P_C depending on the PTM — can be rationalized as follows: in water, the absence of interlayer water removes a structural buffer and exposes the aluminosilicate sheets to unmediated hydrostatic stress, lowering P_C. In PDMS, the encapsulation by the polymer matrix provides an additional mechanical reinforcement, delaying the onset of the structural transition regardless of the hydration state.

The nature of the structural transition in halloysite is likely analogous to that observed in kaolinite and dickite (Hwang et al., 2017; Dera et al., 2003), involving a change in the stacking distance of the aluminosilicate sheets, consistent with the isosymmetric displacive mechanism proposed for dickite by Dera et al. (2003) and the new stacking polytypes identified for kaolinite at comparable pressures (~3.7 and 7 GPa) by Welch and Crichton (2010) using full profile refinement, and further supported by the Raman spectroscopy studies of Basu et al. (2023) and Hong et al. (2022) discussed in Section 3.1 above. Whether this transition is reversible or irreversible in halloysite, and whether it corresponds to the formation of new polytypes, remains to be established by a more detailed structural analysis beyond the scope of the present work: unlike kaolinite, halloysite lacks three-dimensional long-range stacking order, which precludes the kind of full profile/Rietveld analysis used by Welch and Crichton (2010) or Hong et al. (2022) to identify specific polytypes, and we did not perform decompression runs in the present study. A dedicated high-pressure/decompression study of halloysite, ideally combined with vibrational spectroscopy as done for kaolinite, is a natural follow-up to establish the reversibility and detailed character of this transition.

5. Conclusion

In summary, this study provides the first systematic investigation of the pressure-induced structural evolution of halloysite as a function of morphology, hydration state, and pressure-transmitting medium. Our findings demonstrate that their shape fundamentally dictates the response of halloysite to mechanical stress at the nanoscale, revealing three distinct regimes:

1. **A low-pressure regime (P < 0.5 GPa):** Dominated by the rapid and irreversible dehydration of spheroidal halloysite in water environment. The removal of interlayer water leads to a denser, more ordered structure with a higher bulk modulus (up to $B_0 \approx$ 51 GPa for dehydrated spheroidal samples, Table 1).
2. **An intermediate regime (P ~1.5–3 GPa):** Specific to cylindrical halloysite nanotubes compressed in water, where pressure drives active water intercalation into initially anhydrous interlayer spaces. This molecular pump mechanism is absent in spheroidal particles. The intercalated water modifies the balance between the hydrated and anhydrous structural populations but does not strongly alter the c-axis compressibility.
3. **A high-pressure regime** (P_C = **2.5–4.8 GPa**): Both morphologies ultimately undergo a structural instability of the 1:1 aluminosilicate layer, regardless of hydration state. The exact value of P_C is modulated by both the interlayer water content and the PTM, with PDMS generally stabilizing the structure by encapsulation.

These findings demonstrate that the pressure-transmitting medium acts not only as a mechanical stress transmitter but also as a chemical reservoir that significantly alters both the water content and the bulk mechanical properties of the clay particles. The coupling between particle geometry, interlayer water, and surrounding medium controls the pressure response of halloysite nanoparticles. These insights open perspectives for the design of smart nanocontainers capable of responsive fluid uptake or release under mechanical stimuli, with potential applications in high-pressure nanocomposites, drug delivery systems, and as geological indicators for water transport in subduction zones.

Ex-situ recovery and imaging of the compressed particles were not performed in this study: the sample volumes in these membrane-driven DAC experiments are extremely small, and, especially in the presence of a viscous PTM, the powder sample is generally lost or dispersed upon

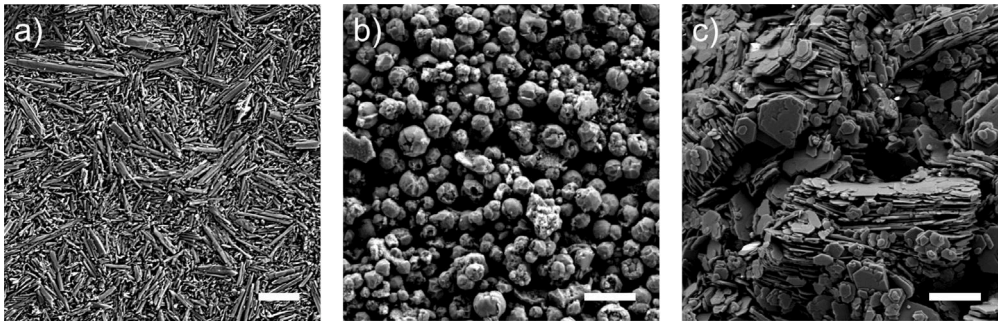

Fig. 6. SEM images of (a) Dragon Mine cylindrical Halloysite, (b) Opotiki spheroidal Halloysite and (c) Kaolinite. The scale bar corresponds to 1 μm.

opening the cell, so that reliable recovery is generally not practically possible with our current setup. Ex-situ imaging of recovered particles — to check for possible radial collapse analogous to what has been reported for imogolite nanotubes (Rouzière et al., 2023, 2024) — would require a dedicated, recovery-optimized experimental protocol and constitutes a natural and informative extension of this work.

CRediT authorship contribution statement

V. Balédent: Writing – review & editing, Writing – original draft, Visualization, Supervision, Resources, Methodology, Investigation, Funding acquisition, Formal analysis, Data curation, Conceptualization. **J. Bodin:** Formal analysis, Data curation. **S. Rouzière:** Writing – review & editing. **P. Launois:** Writing – review & editing. **E. Joussein:** Writing – review & editing, Resources. **E. Paineau:** Writing – review & editing.

Declaration of competing interest

The authors declare that they have no known competing financial interests or personal relationships that could have appeared to influence the work reported in this paper.

Acknowledgments

We acknowledge the MORPHEUS platform at the Laboratoire de Physique des Solides for sample measurement at ambient conditions. This work was financially supported by the Paris Ile-de-France Region in the framework of DIM MaTerRE (project DAC-VX).

Appendix A. SEM images of the samples used in this study

SEM imaging was performed on a Zeiss Sigma 360 scanning electron microscope at 1.5 kV. The sample was prepared by dispersing a few of powder in 2 mL of water under 2 s of ultrasonication. Subsequently, a droplet was deposited onto a silicon wafer and air-dried prior to analysis.

Appendix B. Effect of water medium on halloysite

See Fig. 7.

Appendix C. Kaolinite with water as pressure transmitting medium

See Fig. 8.

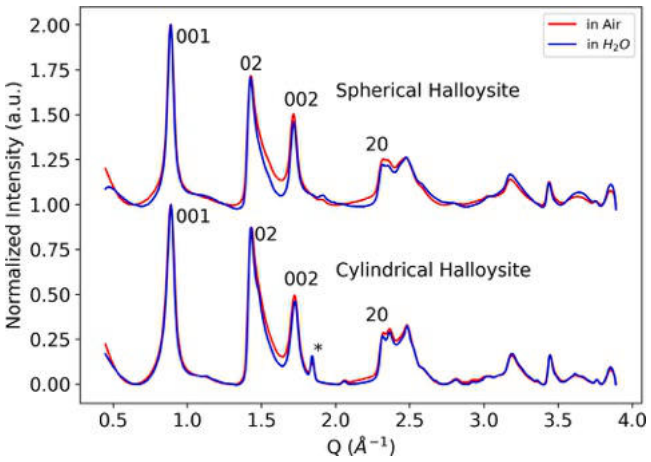

Fig. 7. X-ray diffraction patterns measured at ambient pressure of spheroidal and cylindrical halloysite samples in air (in red) and in water (in blue). The diffractograms are vertically offset for clarity. The star symbol indicates a quartz impurity reflection.

Appendix D. Spheroidal halloysite with water as pressure transmitting medium

See Figs. 9 and 10.

Appendix E. Spheroidal halloysite with Si oil (PDMS) as pressure transmitting medium

See Figs. 11 and 12.

Appendix F. Cylindrical halloysite with water as pressure transmitting medium

See Figs. 13 and 14.

Appendix G. Cylindrical halloysite with Si oil (PDMS) as pressure transmitting medium

See Figs. 15 and 16.

Data availability

Data will be made available on request.

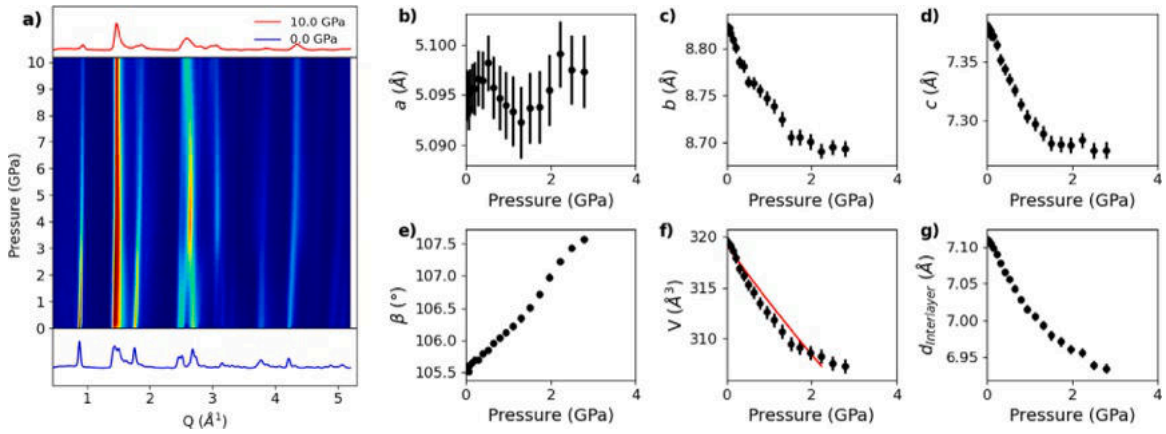

Fig. 8. (a): Color map showing the evolution of the diffractogram of kaolinite as a function of pressure, with water as the transmitting medium. The diffraction patterns at the lowest and highest pressures are displayed below (in blue) and above (in red) the color map, respectively. (b–g): Pressure dependence of the monoclinic lattice parameters *a* (b), *b* (c), *c* (d) and *β* angle (e) (in black). The derived unit cell volume (f) and the interlayer distance (g) are also plotted as functions of pressure.

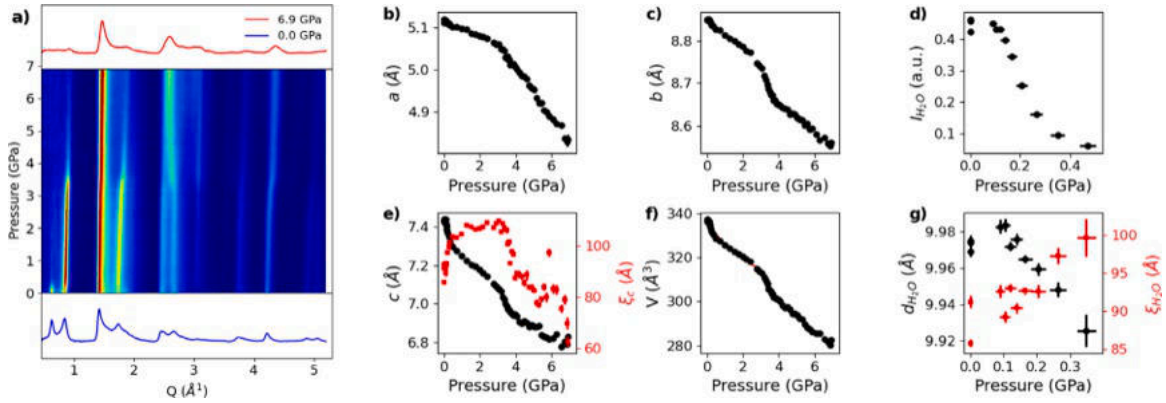

Fig. 9. (a): Color map showing the evolution of the diffractogram of naturally hydrated spheroidal halloysite as a function of pressure, with water as the transmitting medium. The diffraction patterns at the lowest and highest pressures are displayed below (in blue) and above (in red) the color map, respectively. (b, c, e, f): Pressure dependence of the lattice parameters *a* (b), *b* (c), *c* (e), and unit cell volume (f) (in black), and of the correlation length ξ_c of the stacking along *c* (in red, (e)), determined as described in the text. (d, g): The intensity I_{H_2O} of the reflection associated with the hydrated interlayer spacing at 0.63 Å^{-1} is plotted as a function of pressure (d), together with the corresponding distance d_{H_2O} (in black) and its correlation length ξ_{H_2O} (in red) (g).

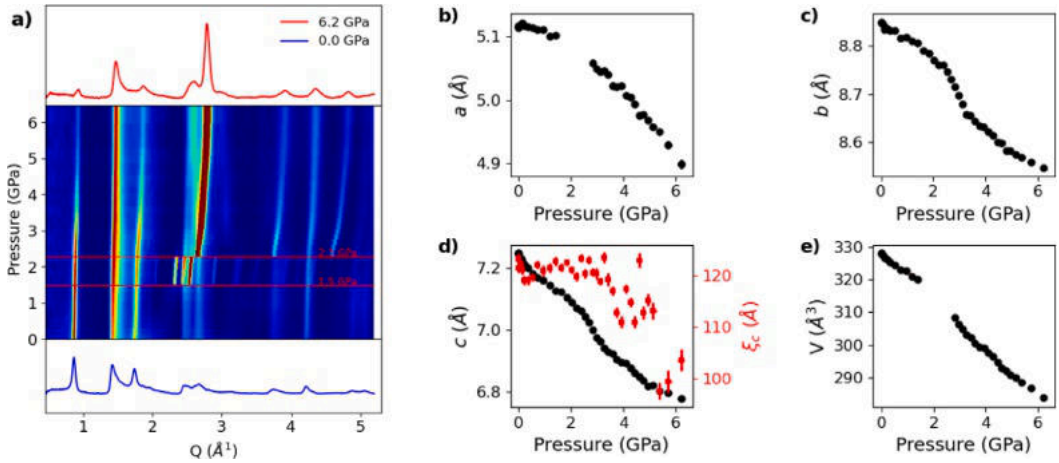

Fig. 10. (a): Color map showing the evolution of the diffractogram of dehydrated spheroidal halloysite as a function of pressure, with water as the transmitting medium. Reflections of ice phase VI, from the bulk water of the PTM, appear at 1.5 GPa and are replaced by reflections of ice phase VII at 2.3 GPa; these two transitions are marked by red horizontal lines. The diffraction patterns at the lowest and highest pressures are displayed below (in blue) and above (in red) the color map, respectively. (b–e): Pressure dependence of the lattice parameters *a* (b), *b* (c), *c* (d), and unit cell volume (e) (in black), and of the correlation length ξ_c of the stacking along *c* (in red, (d)), determined as described in the text.

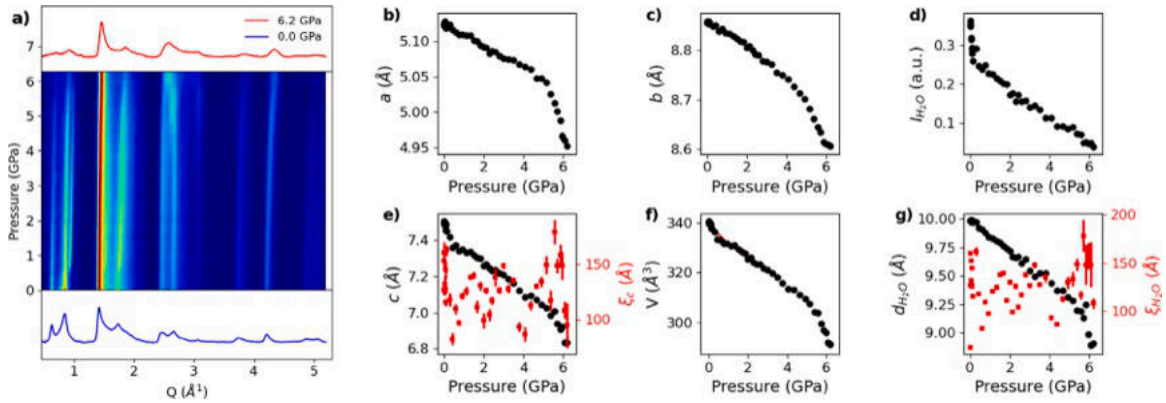

Fig. 11. (a): Color map showing the evolution of the diffractogram of naturally hydrated spheroidal halloysite as a function of pressure, with PDMS as the transmitting medium. The diffraction patterns at the lowest and highest pressures are displayed below (in blue) and above (in red) the color map, respectively. (b, c, e, f): Pressure dependence of the lattice parameters a (b), b (c), c (e), and unit cell volume (f) (in black), and of the correlation length ξ_c of the stacking along c (in red, (e)), determined as described in the text. (d, g): The intensity I_{H_2O} of the reflection associated with the hydrated interlayer spacing at 0.63 Å^{-1} is plotted as a function of pressure (d), together with the corresponding distance d_{H_2O} (in black) and its correlation length ξ_{H_2O} (in red) (g).

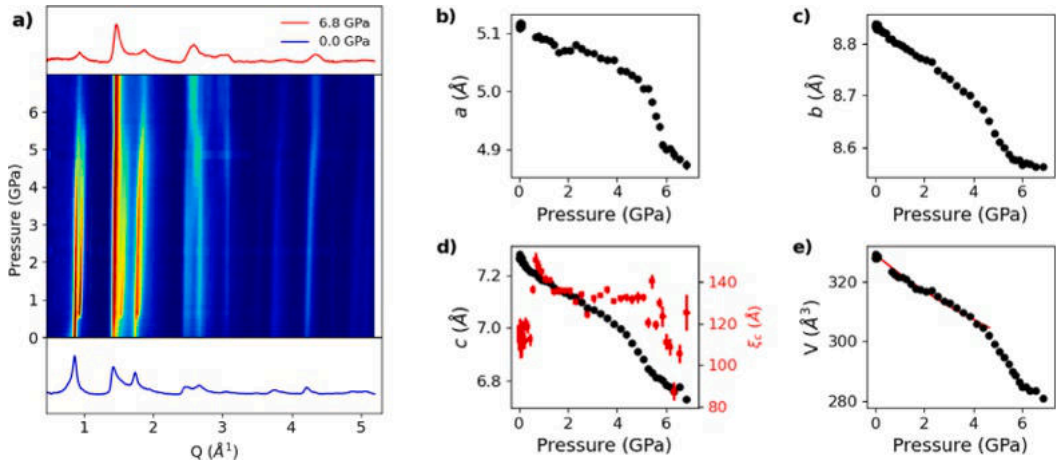

Fig. 12. (a): Color map showing the evolution of the diffractogram of dehydrated spheroidal halloysite as a function of pressure, with PDMS as the transmitting medium. The diffraction patterns at the lowest and highest pressures are displayed below (in blue) and above (in red) the color map, respectively. (b–e): Pressure dependence of the lattice parameters a (b), b (c), c (d), and unit cell volume (e) (in black), and of the correlation length ξ_c of the stacking along c (in red, (d)), determined as described in the text.

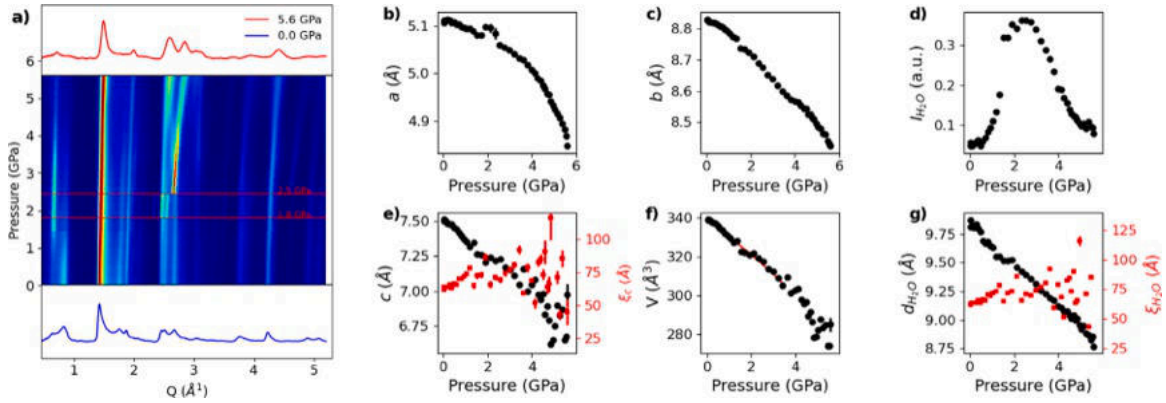

Fig. 13. (a): Color map showing the evolution of the diffractogram of naturally hydrated cylindrical halloysite as a function of pressure, with water as the transmitting medium. Reflections of ice phase VI, from the bulk water of the PTM, appear at 1.5 GPa and are replaced by reflections of ice phase VII at 2.5 GPa; these two transitions are marked by red horizontal lines. The diffraction patterns at the lowest and highest pressures are displayed below (in blue) and above (in red) the color map, respectively. (b, c, e, f): Pressure dependence of the lattice parameters a (b), b (c), c (e), and unit cell volume (f) (in black), and of the correlation length ξ_c of the stacking along c (in red, (e)), determined as described in the text. (d, g): The intensity I_{H_2O} of the reflection associated with the hydrated interlayer spacing at 0.63 Å^{-1} is plotted as a function of pressure (d), together with the corresponding distance d_{H_2O} (in black) and its correlation length ξ_{H_2O} (in red) (g).

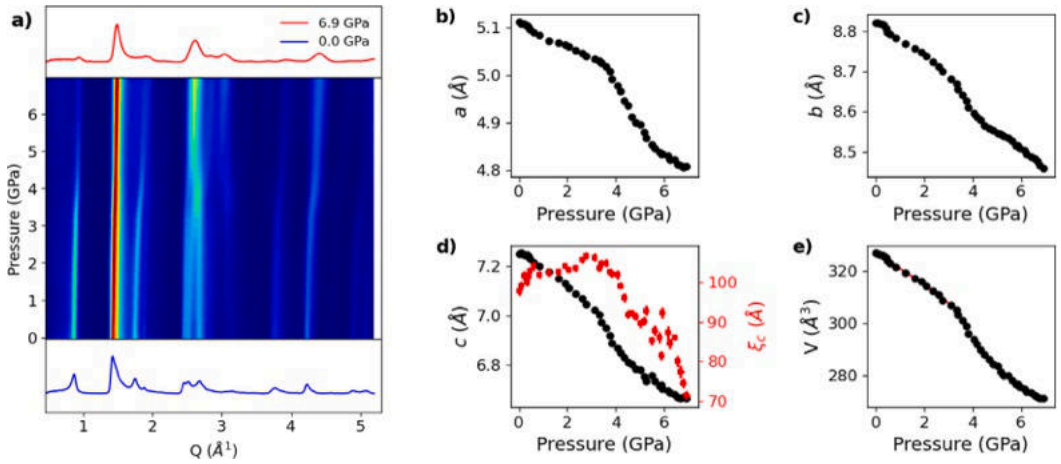

Fig. 14. (a): Color map showing the evolution of the diffractogram of dehydrated cylindrical halloysite as a function of pressure, with water as the transmitting medium. The diffraction patterns at the lowest and highest pressures are displayed below (in blue) and above (in red) the color map, respectively. (b–e): Pressure dependence of the lattice parameters *a* (b), *b* (c), *c* (d), and unit cell volume (e) (in black), and of the correlation length ξ_c of the stacking along *c* (in red, (d)), determined as described in the text.

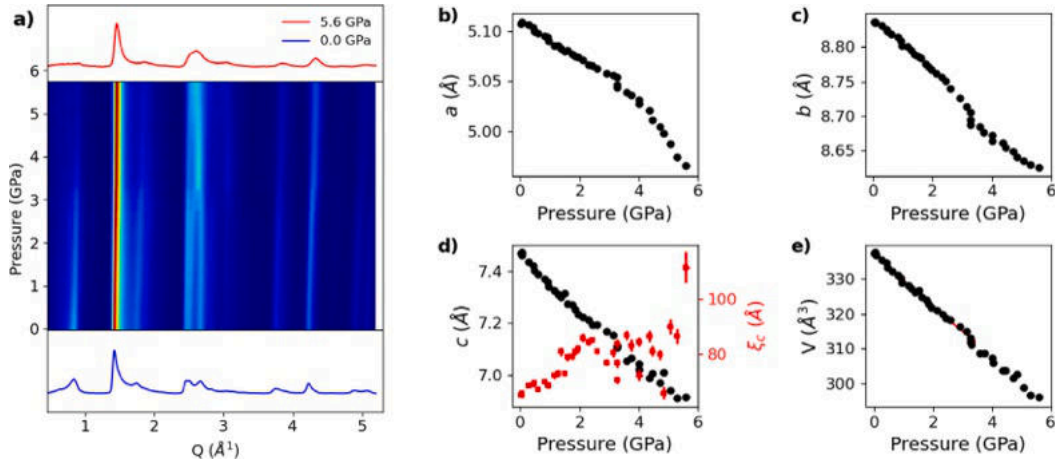

Fig. 15. (a): Color map showing the evolution of the diffractogram of naturally hydrated cylindrical halloysite as a function of pressure, with PDMS as the transmitting medium. The diffraction patterns at the lowest and highest pressures are displayed below (in blue) and above (in red) the color map, respectively. (b–e): Pressure dependence of the lattice parameters *a* (b), *b* (c), *c* (d), and unit cell volume (e) (in black), and of the correlation length ξ_c of the stacking along *c* (in red, (d)), determined as described in the text.

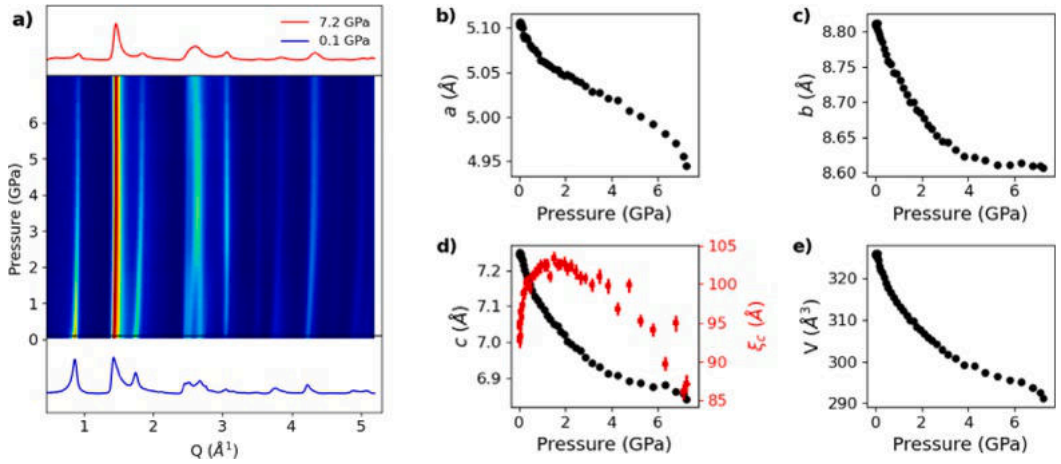

Fig. 16. (a): Color map showing the evolution of the diffractogram of dehydrated cylindrical halloysite as a function of pressure, with PDMS as the transmitting medium. The diffraction patterns at the lowest and highest pressures are displayed below (in blue) and above (in red) the color map, respectively. (b–e): Pressure dependence of the lattice parameters *a* (b), *b* (c), *c* (d), and unit cell volume (e) (in black), and of the correlation length ξ_c of the stacking along *c* (in red, (d)), determined as described in the text.

References

Basu, A., Mookherjee, M., 2021. ACS Earth Space Chem. 5, 834–848.
Basu, A., Mookherjee, M., Clapp, S., Chariton, S., Prakapenka, V.B., 2023. Appl. Clay Sci. 245, 107144.
Boettger, J.C., Honnell, K.G., Peterson, J.H., Greeff, C.W., Crockett, S.D., 2012. AIP Conf. Proc. 1426 (June 2014), 812–815.
Bousige, C., Rols, S., Paineau, E., Rouzière, S., Mocuta, C., Verberck, B., Wright, J.P., Kataura, H., Launois, P., 2012. Phys. Rev. B 86, 045446.
Butler, I.S., Frost, R.L., 2006. Appl. Spectrosc. Rev. 41 (5), 449–471.
Calvino, M.M., Lisuzzo, L., Cavallaro, G., Lazzara, G., Yadav, R.P., Dolgan, K., Lvov, Y.M., 2025. ACS Appl. Bio Mater. 8 (4), 2674–2690.
Churchman, G., Gates, W., Theng, B., Yuan, G., 2006. Dev. Clay Sci. 1, 625–675.
Churchman, G., Whitton, J., Claridge, G., Theng, B., 1984. Clays Clay Miner. 32 (4), 241–248.
Dera, P., Prewitt, C.T., Japel, S., Bish, D.L., Johnston, C.T., 2003. Am. Mineral. 88 (10), 1428–1435.
Ewis, D., Ba-Abbad, M.M., Benamor, A., El-Naas, M.H., 2022. Appl. Clay Sci. 229, 106686.
Goryainov, S.V., Tse, J.S., Desgreniers, S., Kawaguchi, S.I., Pan, Y., Likhacheva, A.Y., Molokeev, M.S., 2021. Phys. Chem. Miner. 48 (10), 36.
Hillier, S., Brydson, R., Delbos, E., Fraser, T., Gray, N., Pendlowski, H., Phillips, I., Robertson, J., Wilson, I., 2016. Clay Miner. 51 (3), 325–350.
Hong, M., Dai, L., Hu, H., Zhang, X., 2022. Am. Mineral. 107 (3), 385–394.
Hwang, H., Choi, J., Liu, Z., Kim, D.-Y., He, Y., Celestian, A.J., Vogt, T., Lee, Y., 2020. ACS Earth Space Chem. 4 (2), 183–188.
Hwang, H., Seoung, D., Lee, Y., Liu, Z., Liermann, H.-P., Cynn, H., Vogt, T., Kao, C.-C., Mao, H.-K., 2017. Nat. Geosci. 10 (12), 947–953.
Joussein, E., Petit, S., Churchman, J., Theng, B., Righi, D., Delvaux, B., 2005. Clay Miner. 40 (4), 383–426.
Kiaee, G., Dimitrakakis, N., Sharifzadeh, S., Kim, H.-J., Avery, R.K., Moghaddam, K.M., Haghniaz, R., Yalcintas, E.P., Barros, N.R.d., Karamikamkar, S., et al., 2022. Adv. Heal. Mater. 11 (7), 2102054.
Lee, Y., Kim, P., Kim, H., Seoung, D., 2020. Materials 13.
McMahon, M.I., 2012. Adv. X-Ray Crystallogr. 69–109.
Monet, G., Amara, M.S., Rouzière, S., Paineau, E., Chai, Z., Elliott, J.D., Poli, E., Liu, L.M., Teobaldi, G., Launois, P., 2018. Nat. Commun. 9.
Naciri, Y., Ghazzal, M.N., Paineau, E., 2024. Adv. Colloid Interface Sci. 103139.
Otunola, B.O., Ololade, O.O., 2020. Environ. Technol. Innov. 18, 100692.
Pan, Y., Joussein, E., Courtin, A., Rouzière, S., Goldmann, C., Vantelon, D., Launois, P., Paineau, E., 2026. Appl. Clay Sci. 287, 108209.
Prescher, C., Prakapenka, V., 2015. High Press. Res. 35 (3), 223–230.
Rouzière, S., Balédent, V., Bodin, J., Elkaim, E., Paineau, E., Launois, P., 2024. Appl. Clay Sci. 254, 107372.
Rouzière, S., Balédent, V., Paineau, E., Elkaim, E., Bizien, T., Nataf, L., Pan, Y., Launois, P., 2023. Inorg. Chem. 62 (2), 957–966.
Siranidi, E., Hillier, S., Chryssikos, G.D., 2024. Clays Clay Miner. 72, e33.
Viseras, C., Cerezo, P., Sanchez, R., Salcedo, I., Aguzzi, C., 2010. Appl. Clay Sci. 48 (3), 291–295.
Volzone, C., 2007. Appl. Clay Sci. 36 (1–3), 191–196.
Warren, B.E., 1941. Phys. Rev. 59, 693–698.
Welch, M.D., Crichton, W.A., 2010. Am. Mineral. 95 (4), 651–654.
You, S., Kunz, D., Stöter, M., Kalo, H., Putz, B., Breu, J., Talyzin, A., 2013. Angew. Chem. Int. Ed. 52 (14), 3891–3895.
Yuan, P., Tan, D., Annabi-Bergaya, F., 2015. Appl. Clay Sci. 112, 75–93.
Zhang, T., Wang, W., Zhao, Y., Bai, H., Wen, T., Kang, S., Song, G., Song, S., Komarneni, S., 2021. Chem. Eng. J. 420, 127574.
Zhou, C.H., Keeling, J., 2013. Appl. Clay Sci. 74, 3–9.